Journal of The Electrochemical Society

Measuring Irreversible Heat Generation in Lithium-Ion Batteries: An Experimental Methodology

To cite this article: Laura Bravo Diaz *et al* 2022 *J. Electrochem. Soc.* **169** 030523

Journal of The Electrochemical Society, 2022 **169** 030523

Measuring Irreversible Heat Generation in Lithium-Ion Batteries: An Experimental Methodology

Laura Bravo Diaz,[1,2,z] Alastair Hales,[1,3] Mohamed Waseem Marzook,[1] Yatish Patel,[1] and Gregory Offer[1,2]

[1]*Department of Mechanical Engineering, Imperial College London, London SW7 2AZ, United Kingdom*
[2]*The Faraday Institution, Quad One, Harwell Science and Innovation Campus, Didcot, United Kingdom*
[3]*Department of Mechanical Engineering, University of Bristol, United Kingdom*

Lithium-ion battery research has historically been driven by power and energy density targets. However, the performance of a lithium-ion cell is strongly influenced by its heat generation and rejection capabilities which have received less attention. The development of adequate thermal metrics able to capture the anisotropic thermal conductivity and uneven internal heat generation rates characteristic of lithium-ion cells is therefore paramount. The Cell Cooling Coefficient (CCC), in $W.K^{-1}$, has been introduced as a suitable metric to quantify the rate of heat rejection of a given cell and thermal management method. However, there is no standardised methodology defining how to measure the heat generation capabilities of a cell. In this study, we applied the CCC empirical methodology to evaluate the rates of irreversible heat generation at various operation conditions, providing maps which give a complete insight into cell thermal performance. The maps derived show how the most important operational variables (frequency, C-rate, SOC and temperature) influence the cell thermal performance. These maps can be used along with the CCC by pack engineers to optimise the design of thermal management systems and to down select cells according to their thermal performance.

 [DOI: 10.1149/1945-7111/ac5ada]

Manuscript submitted November 9, 2021; revised manuscript received March 1, 2022. Published March 16, 2022. *This paper is part of the JES Focus Issue on Women in Electrochemistry.*

Supplementary material for this article is available online

Lithium-ion batteries are becoming increasingly important for ensuring sustainable mobility, and are now the technology of choice for electric vehicles.[1–3] Research into lithium-ion batteries is intensive and wide spread; in order to develop advanced materials required for the technology to meet the demands of the market. However, resources are committed principally to the enhancement of power capability and specific energy at the cell level ($Wh.g^{-1}$) with far less consideration given to how to remove heat.[4,5] This has been shown to lead to suboptimal cells which are prone to large internal thermal gradients which cause accelerated and inhomogeneous degradation.

Cell behaviour is strongly dominated by temperature, since it affects impedance exponentially.[6] A badly designed cell from a thermal management perspective will lead to reduced power, less usable capacity, and ultimately reduced useable energy at pack level. Despite the strong dependency of lithium-ion cell performance on temperature, the information battery suppliers and manufacturers provide regarding the effect of temperature on battery performance is not standardised, and is rarely sufficient to characterise a given battery's performance across the full temperature operating range, as defined by the same manufacturer. Additionally, there is insufficient information on typical cell spec sheets to inform how easy it is to reject heat from a cell, nor sufficient information on heat generation to guide pack design.

In response to this need, a new metric to evaluate the ability of lithium-ion cells to reject heat, independent of their chemistry, form factor or manufacturer has been recently developed.[5] The cell cooling coefficient, or CCC ($W\ K^{-1}$), which can be measured empirically via standardized experiments, quantifies the heat rejection capability of a cell for a particular thermal management method, i.e. via the tab[7] or surface cooling.[8] The evaluation of a given cell's thermal performance using this metric avoids the use of unjustifiable assumptions required to calculate the Biot number or the thermal conductance of the cell. These conventional heat rejection measures are not suitable for its application in lithium-ion cells since they do not consider the anisotropic thermal conductivity and the uneven heat generation characteristic of these electrochemical devices. The CCC remains a metric which must be independently evaluated for traceability, but the performance of the apparatus to repeatedly determine the rate of heat rejection from a cell which is generating heat at a constant rate, and is not imposed to transient thermal conditions, using a specified thermal management method (i.e. surface cooling or tab cooling in a pouch cell) has been demonstrated. The apparatus for the CCC is low-cost and the experiments can be conducted with any battery cycler and in any battery laboratory, making the CCC apparatus concept an attractive alternative for long term experimental studies, where isothermal calorimeters are not available or financially justifiable.

The design of a battery thermal management system should consider the heat rejection capability of a cell among many other factors, such as the cooling method strategy, size, weight, material, and amount of coolant, all of which have an influence on the cost and performance of the system. However, one of the most important battery characteristics that must be understood for the design of an adequate thermal management system is the heat generation rate of the battery.[9] A capability for the battery to effectively reject heat is important, but the battery manufacturer should also focus on minimising the rate of heat generation—this will reduce the burden on the thermal management method and reduce the sensitivity of the battery's heat rejection capability on overall battery performance.

Heat is generated within a cell during operation due to irreversible and reversible electrochemical processes at the pore-scale, as described through Eq. 1.[10–12] The first term in Eq. 1 corresponds to the irreversible heat rate and the second represents reversible heat rate, where I is current passing through the cell, OCV is the cell open circuit potential, V is cell potential, T is the cell temperature, ΔS is the entropy change, n is the number of electrons transferred in the electrochemical reaction and F refers to the Faraday constant.

$$\dot{Q}_{gen} = \dot{Q}_{irrev} + \dot{Q}_{\text{rev}} = I \cdot (OCV - V) - \left(I \cdot T\frac{\Delta S}{n \cdot F}\right) \qquad [1]$$

[z]E-mail: l.bravo-diaz@imperial.ac.uk

The irreversible heat is a consequence of the losses due to the difference between the cell open-circuit potential and the operating potential and includes the ohmic, kinetic and mass transport heat corresponding to the ohmic, kinetic and mass transport overpotentials, as can be seen in Fig. 1.[9,13]

The ohmic heat is related to long-range interactions, i.e. joule heating from electron and ionic flow resistance within the electrodes and electrolyte, contact resistance and solid electrolyte interphase (SEI) resistance. The kinetic heat is related to short-range interactions, i.e. charge-transfer reactions at the interphase, availability of species and availability of reaction sites.[14,15] The mass transport heat refers to mass transport limitations in the electrodes or electrolyte and temporary build-up of concentration gradients, linked to reaction sites. By contrast, the reversible heat is dominated by the entropy change associated with material phase changes in the cell.

As the cell is operated, the heat generation rates change in response to the evolution of chemical, electrochemical and thermal states.[14] Consequently, the heat generation rate of the battery is dependent on many factors such as state of charge (SOC), applied C-rate, temperature and state of health (SOH).[9] Whilst the CCC can describe the heat rejection capabilities of a cell for a thermal strategy with a single parameter, the quantification of the heat generation rate of a cell is a much more complex issue since it varies significantly with multiple operation variables.

Any method to estimate battery heat generation rate, either numerical or experimental, will have an error attached to it. This error presents uncertainty, which ultimately must be built into the design of the battery thermal management system—failure to do so would risk having a battery pack at risk of generating heat faster than it is able to reject it.[16] If this measurement error is large, the resulting thermal management system is likely to be excessive in performance capability, thus diminishing the energy density of the battery pack as a whole. Reducing this error would therefore provide means to more accurately specifying the performance requirements for the battery thermal management system at an early stage of design. Fundamental understanding of the heat generation rate of a cell is therefore key for battery pack designers, not only to design an adequate thermal management system but also for selecting suitable cells for a target application from the thermal performance perspective. A way to get fundamental understanding on the heat generation rate of a particular cell is to develop a physics based electrochemical thermal model.[9,14,15,17–19] However, these models are complex, cell-specific, require many parameters and need validation experiments. Despite its simplicity, the application of an empirical approach to investigate the heat generation capability of lithium-ion cells and the influence of operational variables has not been widely explored. There are few experimental studies on the quantification of heat generation from individual cells.[11,20–22] These studies often focus on a particular cell model or chemistry and describe the performance of a series of time-consuming experiments to analyse the heat generation of a specific cell. The establishment of a standardised empirical methodology which can directly monitor cell heat generation rates can be beneficial to industry, by minimising the requirement for computationally expensive modelling or time-consuming experiments in the early stages of thermal management system design.

In the present study, an empirical methodology is proposed to evaluate the heat generation rate of a lithium-ion cell across a complete range of operation conditions. The aim is to give battery pack designers a valuable tool to quantify the heat generation capabilities of a cell, coupling heat generation with the CCC. This cell heat generation methodology has been applied to a Custom cell —this provides a benchmark for the battery industry since the physical and thermal properties, as well as the exact composition, are known. The empirical methodology allowed the construction of heat generation rate maps which gave a full insight into how the most important operational variables (frequency, C-rate, SOC and temperature) influence the thermal performance of the cell. The functionality of these maps in combination with the CCC is demonstrated in a worked example, demonstrating the requirements of the thermal management system necessary to maintain the cell below a safe temperature.

Experimental

The methodology employed in this research work is based on the apparatus developed in previous works for determining the CCC for both tab (CCC_{tab})[7] and surface cooling ($CCC_{surface}$)[8] with additional features. These apparatuses are based upon the fundamental principle of a purely conductive system. Each conductive system contains heat sinks, where heat is removed from the domain using Peltier Elements (PEs) and a secondary cooling loop. The rate of heat rejection from the cell tabs is determined by evaluating the temperature difference recorded by the thermocouples positioned along the busbars, as shown in Fig. 2a, and using this difference alongside the material and geometric properties of the busbars to calculate heat rate. The heat rejection from the surface is measured down the brass fins with thermocouples and by using PEs as observed in Fig. 2b. A similar apparatus combining both thermal strategies, controlling surface and tabs, has been applied to investigate heat generation within the cell.

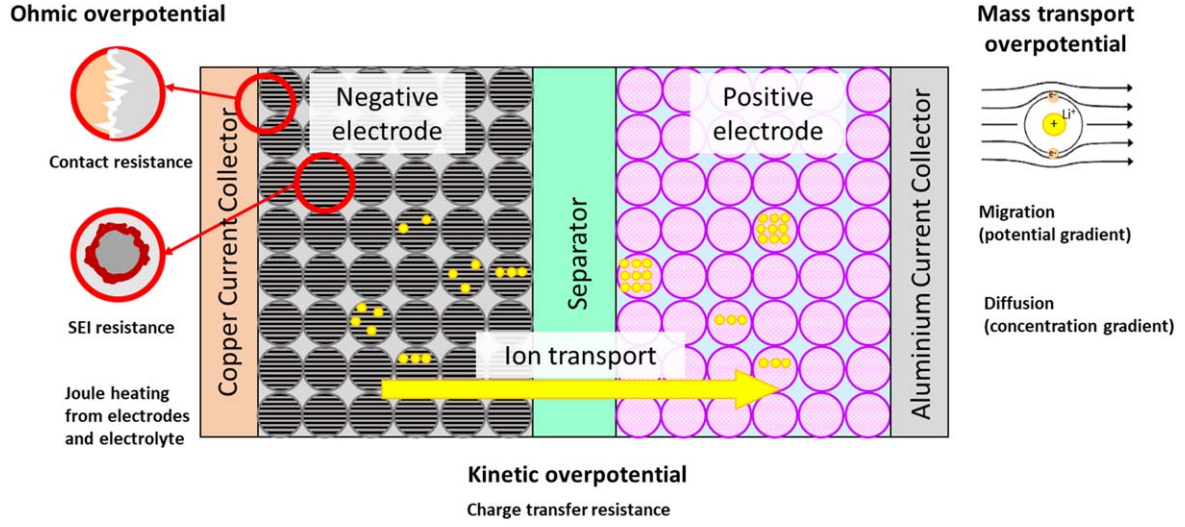

Figure 1. Schematic of the lithium-ion discharge process considering the internal behaviour of a cell and the components associated to the irreversible heat (ohmic, kinetic and mass transport).

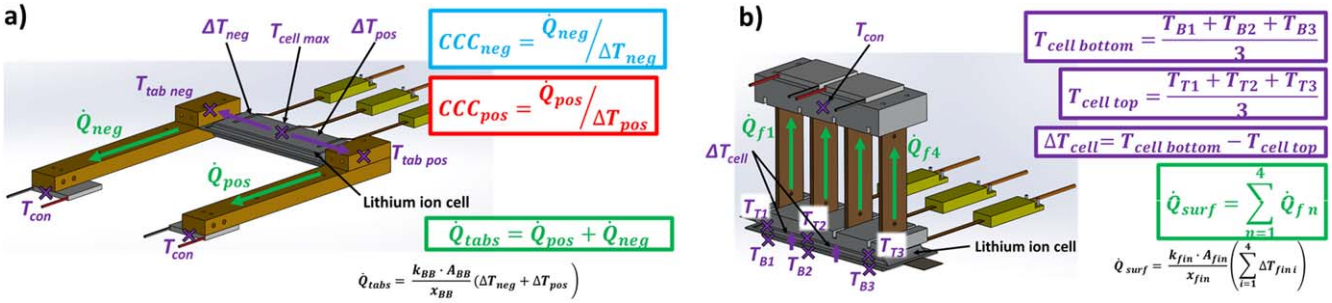

Figure 2. (a) Apparatus for the determination of the CCC_{tabs}, (b) Apparatus for the determination of the CCC_{surf}.

Apparatus.—Detailed images on the construction of the apparatus are shown in Fig. 3. The insulation (Celotex CW3000, 0.023 W $m^{-1}K^{-1}$) which encases the apparatus is required to ensure that heat losses through other pathways beside the prescribed heat sinks are minimised. The cell sat within the bottom insulation shell. It was also mounted between brass clamps connected to brass busbars with a PE at their ends to monitor the heat rejection from the tabs. The tabs were connected to the clamps via thermal interface gel (8 $W.m^{-1}.K^{-1}$). The top surface of the cell is in contact with a surface cooling rig[8,23] also via the thermal interface gel. The surface cooling rig is enclosed on the top insulation shell and is composed of a base aluminium plate (180 $W.m^{-1}K^{-1}$), four integrated brass fins and a top aluminium plate with 2 PEs to evaluate the heat rejection from the surface. An additional aluminium plate with a single PE is located in the bottom insulation shell, below the cell, to minimise thermal losses as can be observed in Fig. 3.

A complete schematic of the experimental apparatus and the thermocouple locations is shown in Fig. 4. A total of 21 K-type thermocouples (TCs) were used, one in each clamp (TC7 and TC8), two on each of the four brass fins (TC9 - TC16), three in each busbar (TC17, TC18 and a Control TC on the positive busbar and TC19, TC20 and a Control TC on the negative busbar), one Control TC on the top aluminium plate, one Control TC on the bottom aluminium plate, one TC to monitor the ambient, and three thin-leaf K-type TCs on each side of the cell, in pairs, (TC1–TC6). All TCs except for those on the cell were adhered using thermal epoxy (1.22 $W.m^{-1}K^{-1}$). The three thin-leaf K-type TCs (TC1–TC3) placed on the top cell surface were held in place using thermally conductive Kapton tape. TC1–TC3 had a thickness of 50 μm and a width of 3.2 mm, ensuring good contact between the cell and the aluminium base plate. The consistency of this interface was further ensured using a layer of 0.5 mm thick thermal interface gel. TC4–TC6 were also adhered to the bottom surface of the cell with Kapton tape. The temperature at the site of each TC was recorded at 1 Hz using a Pico TC-08 datalogger.

The entire apparatus was placed in an ESPEC environmental chamber (Model: BPL-3) to ensure fine temperature control of the apparatus. This was critical for achieving thermal equilibrium through the apparatus prior to each test. The Control TCs show the heat sinks, the sites where the temperature was controlled (Fig. 4). The PEs at the end of the busbars were used to set the control temperature for the tab conductive system boundary. These PEs were set to the same temperature of the thermal chamber ($T_{control}$), which is recorded just before the start of each test. The PEs adhered to the top surface of the top plate were used to set the control temperature for the surface conductive system boundary. This temperature was also set to the same temperature of the environmental chamber ($T_{control}$). The bottom aluminium plate is included to replicate the concept presented by Hales et al.[23] The PE on the bottom plate was set to be 0.25 °C colder than the bottom surface of the cell. Consequently, the bottom plate heated up as the cell heated up. This control strategy allowed measuring the heat rejected from the cell surface minimising thermal losses.

The apparatus is designed to measure the rate of heat extraction from the entire conductive system and therefore, when the system is not in a transient thermal state, the rate of heat extraction must, through energy-balance, be equal to the rate of heat generation. This assumption is central to the analysis conducted in the present investigation, and is verified through experiments conducted in previously published work.[8] Using a resistive heater adhered to the test cell (which was not under any load), and thus knowing the exact rate of heat generation from the resistive heater since the power input was controlled, it was found that of the 1.50 W of heat added to the system (through the resistive heater), 1.42 W of heat was recorded being rejected from the system, along the specified heat rejection pathways built into the apparatus. This represents an error of 5.4%, and this error may be used in the present study since the apparatus is conceptually similar and the test cell is geometrically similar. Given the low error, loss fractions are not built into the analysis in the present study—the assumption is made that any heat losses that do occur are consistent across different tests and thus do not affect the qualitative analysis.

The current was supplied to the cell from a Bio-logic (BCS 815) battery cycler through connections to the long busbars attached to either tab at the clamp subassembly. In a previous investigation, it was found that the ohmic heat generation, due to contact resistances in the clamp subassembly, was not negligible.[23] The current-carrying connection of the busbar to the cell cycler has been set far from the cell and next to the site of PE thermal control to mitigate this effect, as can be seen in Figs. 3b and 4. The busbar-tab connection interface did not induce a significant contact resistance because of the large surface area and clean, polished busbar surfaces. The unknown rate of heat removal and heat gain from the cell into the current carrying cables was another limitation of the original apparatus.[7] The voltage sense connection, which carries negligible current and therefore does not induce ohmic heating at material interfaces, was kept close to the cell to maximise the accuracy of the measurement.[23]

Cell properties.—A pouch-type custom made cell manufactured by Customcells Itzehoe GmbH was used for this work. It contains a graphite anode and a $LiNi_{0.6}Mn_{0.2}Co_{0.2}O_2$ (NMC-622) cathode. The cell has a rated capacity of 17 Ah. The stack has overall dimensions of L 11.7 mm × W 10.1 mm × T ~11.5 mm. The cell tabs are positioned at counter side of the cell with a length of 21 mm, a width of 70 mm, and a thickness of 0.2 mm. The detailed dimension is shown in the Supplementary Information (SI).

Experimental procedure.—The experimental procedure is based on the procedure detailed in previous works for determining the CCC.[7,8,23] The cell heat generation rate ($\dot{Q}_{gen}$) at an specific operation point was measured by inducing conditions on the cell where each variable that affects $\dot{Q}_{gen}$ is kept constant. These variables are frequency, current magnitude or C-rate, SOC, and operating temperature. A square wave pulsing current profile was used to induce heat generation in the cell under test. The amplitude of the square wave (I_{pulse}) was kept constant over a test and the

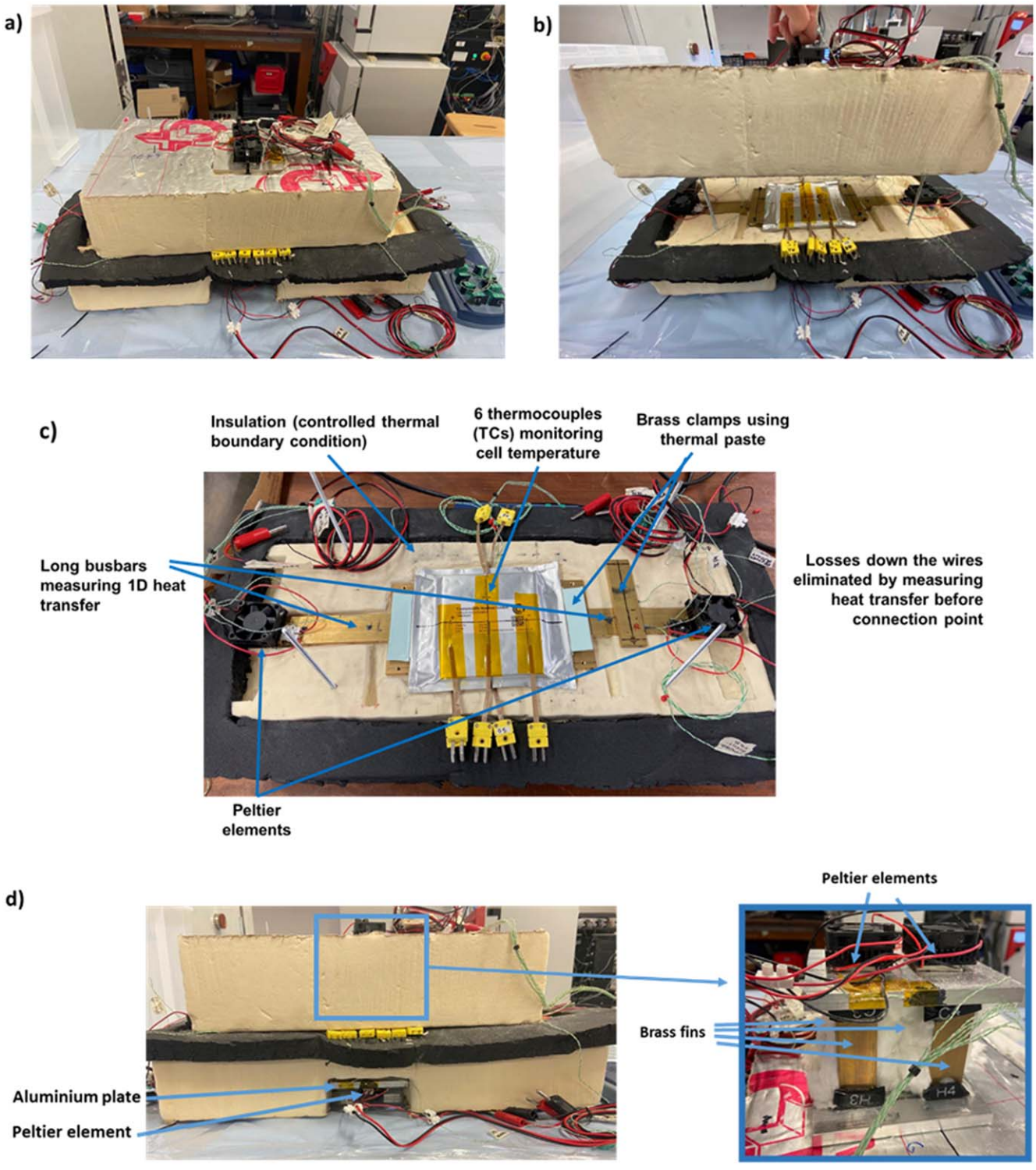

Figure 3. Experimental apparatus setup: (a) Cell enclosed in the apparatus ready for electrical connection and placement in a thermal chamber, (b) View of the bottom insulation shell when opening the apparatus, (c) Components in the bottom insulation cell (d) Front view of the apparatus with a detail of the surface cooling rig in the inset.

current square wave profile was centred such that $I_{average} = 0$ A for the duration of each pulsing period, maintaining a constant time-averaged cell SOC. In this way, the irreversible heat generation rate of a cell at a specific operation point was possible to measure. The pulsing profile was applied for an extended period of time, allowing the cell to heat up within the conductive system and reach a steady state temperature, elevated above $T_{control}$. Once this state is reached, the requirements for a constant $\dot{Q}_{gen}$ are reached. The OCV was taken at the start and end of each test, at $T_{control}$, to verify no change to the initial SOC. The full procedure is described below. It includes a beginning-of-cycle rest period and an end-of-cycle cell characterisation procedure, to ensure no measurable degradation was occurring between tests.

1. 8 h rest, setting the ambient temperature of the environmental chamber to $T_{control}$ with no other temperature control applied,

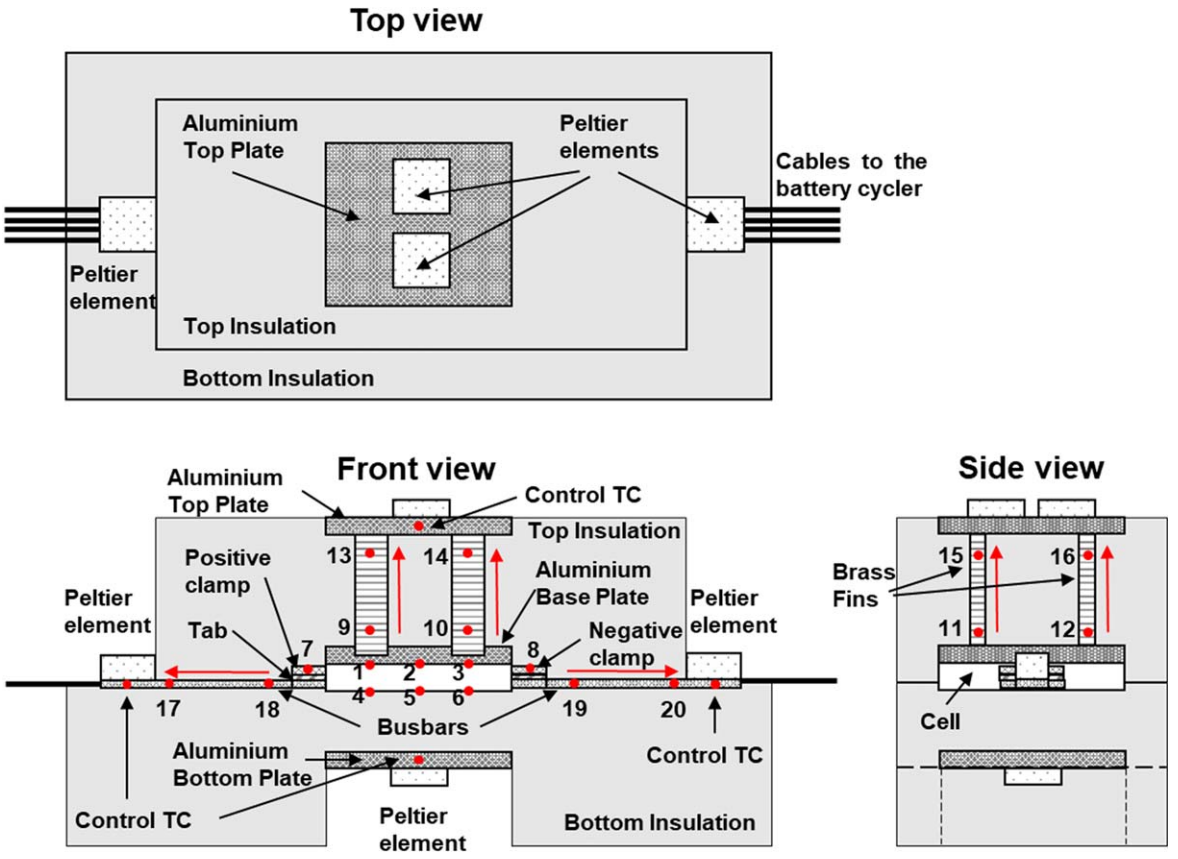

Figure 4. Schematic of the experimental apparatus and the thermocouple locations.

allowing the entire conductive system to reach a thermal equilibrium. This is essential to set the datum temperature for each TC dataset.
2. Temperature control system switched on, to achieve $T_{control}$ for the test (recorded from the ambient TC in the environmental chamber).
3. Square wave current pulsing at a fixed frequency, centred around zero and with test specific current magnitude, for 10 h (see Table I).
4. 10 h rest to reach consistent thermal conditions prior to degradation analysis.
5. 1 C CC-CV charge to 4.2 V with a C/100 cut-off, followed by 1 h rest.
6. 1 C CC discharge to 2.7 V for degradation analysis, followed by 1 h rest.
7. 1 C CC-CV charge to 4.2 V with a C/100 cut-off, followed by 0.5 h rest.
8. 1 C discharge to 50% SOC, followed by a 2 h rest.

A total of 69 tests were conducted on three test cells. The four variables (frequency, C-rate, SOC and operating temperature) were studied independently, and a heat generation rate map was constructed for each individual variable. Each point in the heat generation rate maps was obtained by a single test keeping all the variables constant and each map was constructed by a series of tests, only changing one single variable, keeping all the others constant as detailed in Table I.

Data processing.—The data processing procedure introduced below is based on one detailed in previous works.[7,8,23] This procedure is only valid when the cell is in steady state, specifically when the rate of temperature change within the entire conductive system is negligible. This steady state is achieved when $\dot{Q}_{gen}$ is equal to the rate of heat rejection from the system. Consequently, transient heating and cooling effects are not contributing to the temperature gradients recorded within the conductive system.

The apparatus achieved an elevated steady state temperature at approximately 2 h from the start of the pulsing profile. From this point until the end of the pulsing profile, the whole apparatus is in an elevated thermal equilibrium state. For data processing, the mean value, across the elevated thermal equilibrium state period, was taken for each dataset.

$\dot{Q}_{gen}$ is calculated by adding the heat rejection rate from each conducting system ($\dot{Q}_{tabs}$ and $\dot{Q}_{surf}$) and these are determined through the temperature gradient incurred within the prescribed heat rejection pathways. For the tab conducting system, $\dot{Q}_{tabs}$ is sum of the heat rejected from each tab ($\dot{Q}_{pos}$ and $\dot{Q}_{neg}$) and is defined by Eq. 2, where $\Delta T_{BB\ pos}$ is the difference between TC18 and TC17, and $\Delta T_{BB\ neg}$ is the difference between TC19 and TC20. K_{BB} is the thermal conductivity of the busbars (123 W m^{-1}K^{-1}), A_{BB} is the cross-sectional area of each busbar (190.5 mm^2), and x_{BB} is the distance between TC18 and TC17 or TC19 and TC20, for the positive and negative busbars respectively (105 mm).

$$\dot{Q}_{tabs} = \frac{K_{BB} \cdot A_{BB}}{x_{BB}} (\Delta T_{BB\ pos} + \Delta T_{BB\ neg}) \quad [2]$$

For the surface conducting system, $\dot{Q}_{surf}$ is calculated through the temperature gradient present in each of the four fins (i.e. $\Delta T_{fin\ 1} = T_{TC9} - T_{TC13}$). $\dot{Q}_{surf}$ results from the sum of the heat rejected from each fin and is defined by Eq. 3, where K_{fin} is the thermal conductivity of the fins (123 W m^{-1}K^{-1}), A_{fin} is the cross-sectional area of each fin (80.65 mm^2), and x_{fin} is the distance between TCs on each fin (65 mm).

Table I. Summary of all tests in the present investigation.

Variable studied	Frequency/Hz	C-rate/h^{-1}	SOC/%	Temperature/°C
Frequency	62.50000	2.0 C	50	25.78
	6.25000			
	0.62500			
	0.06250			
	0.00625			
		1.0 C (17 A)		
		1.5 C (25.5 A)		
C-rate	0.62500	2.0 C (34 A)	50	25.75
		2.5 C (42.5 A)		
		3.0 C (51 A)		
			50	
			80	
SOC	0.62500	2.0 C	60	25.64
			40	
			20	
				5.86
				10.86
				15.69
Temperature	0.62500	2.0 C	50	20.65
				25.55
				30.52
				35.49
				40.52

$$\dot{Q}_{surf} = \frac{K_{fin} \cdot A_{fin}}{x_{fin}} \left(\sum_{i=1}^{4} \Delta T_{fin\ i} \right) \quad [3]$$

An example of the use of these equations on the data processing is shown in Fig. 5 where the total irreversible heat generation is calculated for an operation point.

Results and Discussion

As briefly described earlier, heat generated within the battery is caused by the energy losses from the conversion of the chemical energy into useful electrical energy by the electrochemical oxidation/reduction reactions and the transport of charged species. These losses occur when a load current, accompanying the electrochemical reactions, flows through the electrodes. This phenomenon is also referred to as "polarization."[24] These losses include[24–26]:

1) Activation losses, also referred to as "activation polarization," and are due to kinetic limitations, e.g. resistance to chemical reaction, availability of species and availability of reaction sites.
2) Ohmic losses, also referred to as "ohmic polarization," due to flow limitations, e.g. resistance to electron flow and resistance to ionic flow.
3) Diffusion losses, also referred to as "concentration polarization," due to mass-transport limitations associated with the temporary build-up of concentration gradients.

All these losses are reflected in the resulting voltage of a cell as shown in Eq. 4, where OCV is the open circuit voltage, resulting from the difference between the electrostatic potential of the two electrodes, and η_{kinetic}, η_{ohmic} and η_{diff} are the kinetic, ohmic and mass transport (diffusion) overpotentials, respectively.

$$V_{Cell} = OCV + \eta_{kinetic} + \eta_{ohmic} + \eta_{diff} \quad [4]$$

Each loss mechanism can be represented by a resistance or impedance across which the overpotential occurs. In the case of the kinetic overpotential the relationship between the overpotential and the current density is given by the Butler-Volmer equation, shown as Eq. 5; where i_0 is the exchange current density of the reaction at standard concentration, α is the charge transfer coefficient, n is the number of electrons transferred in the electrochemical reaction, T refers to temperature and the constants R and F have their usual meaning. The often-referred effective charge-transfer resistance (R_{CT}) results then from the approximation in Eq. 6.

$$i = i_0 \cdot \left\{ \exp\left[\frac{\alpha n F \eta_{kinetic}}{RT} \right] - \exp\left[\frac{(1-\alpha) n F \eta_{kinetic}}{RT} \right] \right\} \quad [5]$$

$$R_{CT} = \frac{\eta_{kinetic}}{i} \quad [6]$$

Similarly, the ohmic and diffusion overpotentials can also be expressed as a function of a resistance and current as presented in Eqs. 7 and 8, respectively.

$$\eta_{ohmic} = R_0 \cdot I \quad [7]$$

$$\eta_{diff} = R_{diff} \cdot I \quad [8]$$

Combining these equations with Eq. 1, we could express the irreversible heat generation rate term as a function of these overpotentials as shown in Eq. 9[27]:

$$\dot{Q}_{gen} = \frac{I}{V} \left(\eta_{kinetic} + \eta_{ohmic} + \eta_{diff} - \frac{T \cdot \Delta S}{n \cdot F} \right) \quad [9]$$

We can observe from Eq. 9 that the heat generation rate will vary accordingly with changes in these overpotentials, and these are greatly influenced by the operating conditions of the lithium-ion cell. Therefore, by varying the operating point, we can introduce significant changes in the overpotentials and study the implications on the heat generation rate of a cell to evaluate its heat generation.

We present here the effects on the heat generation rate when varying the cell operation conditions by means of heat generation maps. The response on the heat generation rate was evaluated by

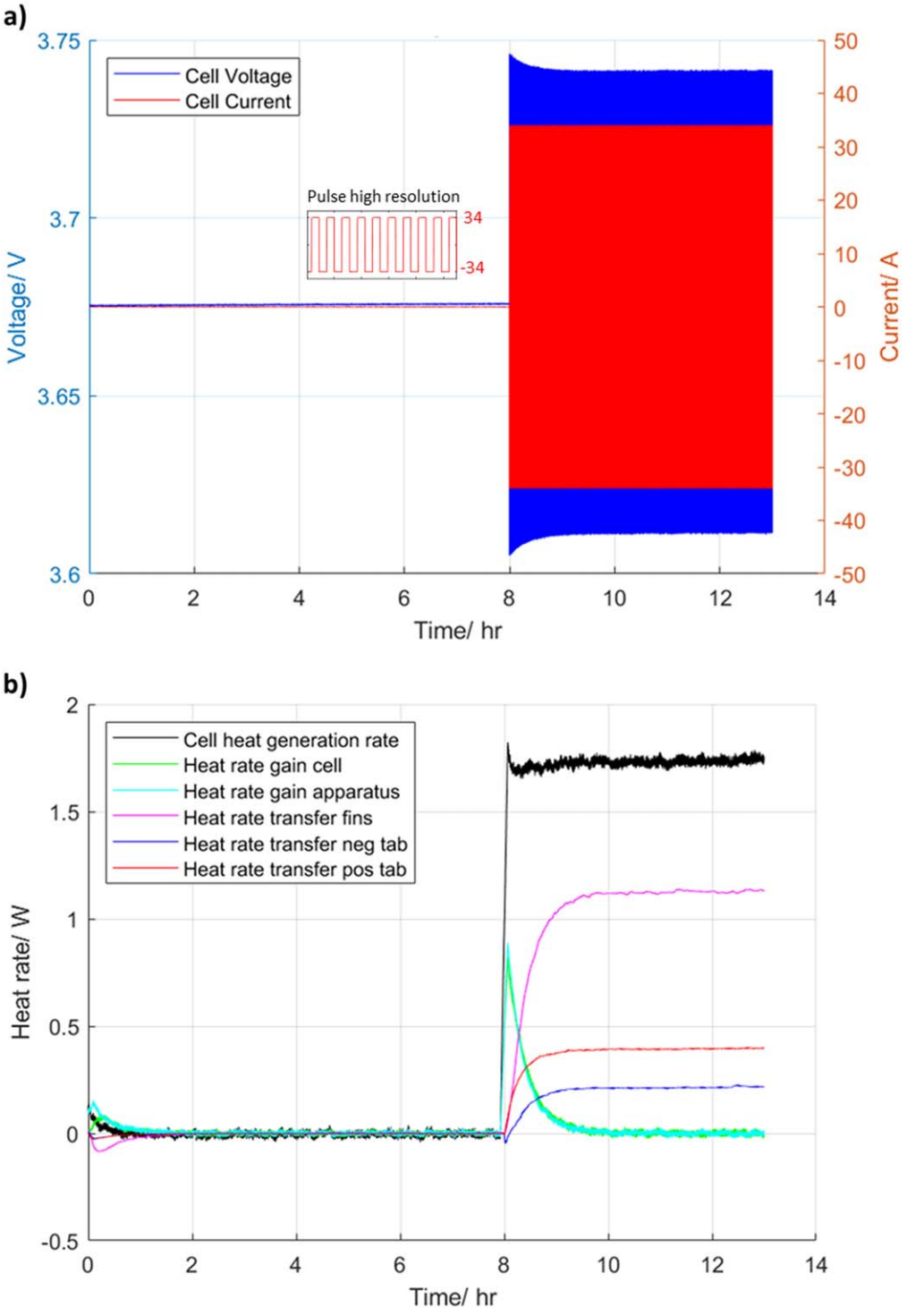

Figure 5. (a) Current and voltage profile over a single test, (b) Heat rate profile over a single test.

studying independently the following variables: frequency, current, temperature, SOC and SOH.

Frequency study.—The numerous mechanisms within the electrochemical processes governing lithium-ion batteries have characteristic times that span many orders of magnitude, as can be observed in Fig. 6. Some experimental techniques, such as Electrochemical Impedance Spectroscopy (EIS),[24–26,28,29] Thermal Impedance Spectroscopy (TIS)[30–33] or Galvanostatic Intermittent Titration (GITT)[24,34] use this principle to their advantage. By analysing the frequency spectrum of a system response it is possible to separate the influence of the processes with differing time constants that occur simultaneously in the time domain. From the knowledge gathered from these techniques, we can distinguish three regions in which different electrochemical processes occur, each region associated to a frequency range:

1) Low frequency range ($f < 1$ Hz): diffusion processes (R_{diff}), thermal transients, degradation mechanisms such as SEI layer growth or lithium plating, self-discharge, electrode mechanical failure.

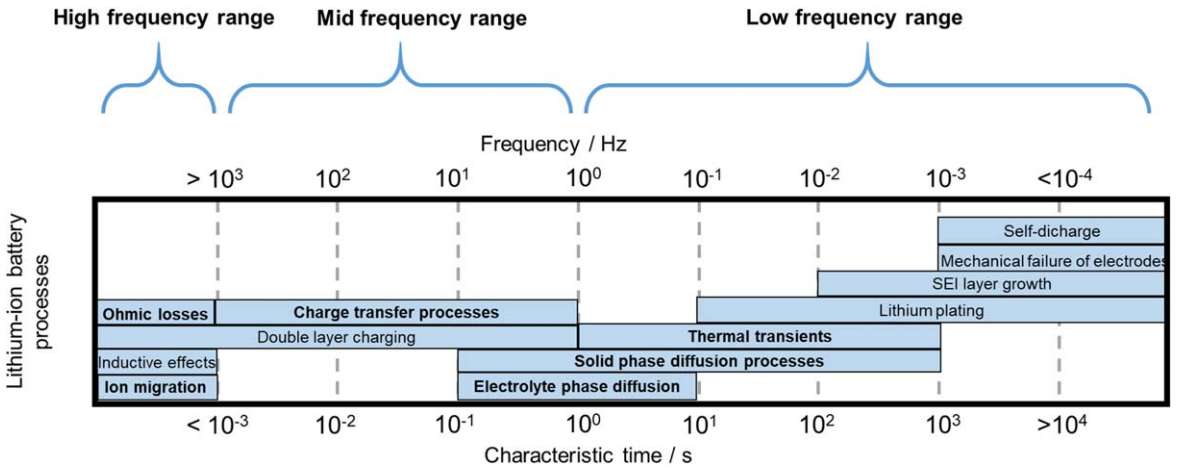

Figure 6. Lithium-ion electrochemical processes and time scales.

2) Mid frequency range (1 Hz $<$ f $<$ 1 kHz): charge transfer reactions (R_{CT}) and double layer effects at anodes, cathodes and solid electrolyte interphases (SEIs).
3) High frequency range (f $>$1 kHz): inductive effects of the connecting wires, resistance of electrolyte and electrodes known as ohmic losses (R_o), ion migration.

Taking all this into account, we can anticipate that the heat generation rate will be a function of frequency as the contributions from the kinetic, and diffusion overpotentials will vary with the characteristic time scale we are at.

First, the influence of the pulsing frequency on the heat generation rate in the lithium-ion cell was studied. Figure 7 shows the heat rates measured at different frequencies, using pulsing time scales from milliseconds to hundreds of seconds. The cell was previously set to 50% SOC and this SOC was kept constant over the whole experiment as the charging and discharging pulses were equal in duration for each frequency studied. The cell was characterised over a series of charges and discharges in between each pulsing period, as can be observed in Fig. 7. The capacity of the cell was not affected over the set of experiments. The SOC was always reset to 50% SOC before each pulsing period. The ambient temperature was also fixed to 25 °C (see Table I).

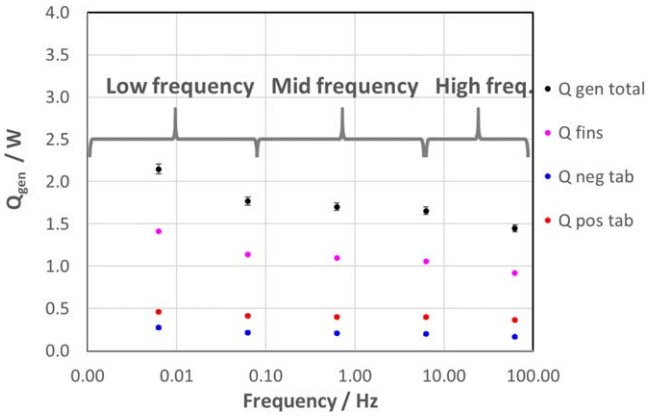

Figure 8. Heat generation rate vs pulsing frequency.

The total heat generation rate of the cell is depicted in black in Fig. 7, and it is the sum of all heat rates measured using the apparatus described in the experimental section: (1) heat rate gained by the cell (in green), (2) heat rate gained by the apparatus (in light blue), (3) heat rate dissipated through the cell surface (in pink), (4)

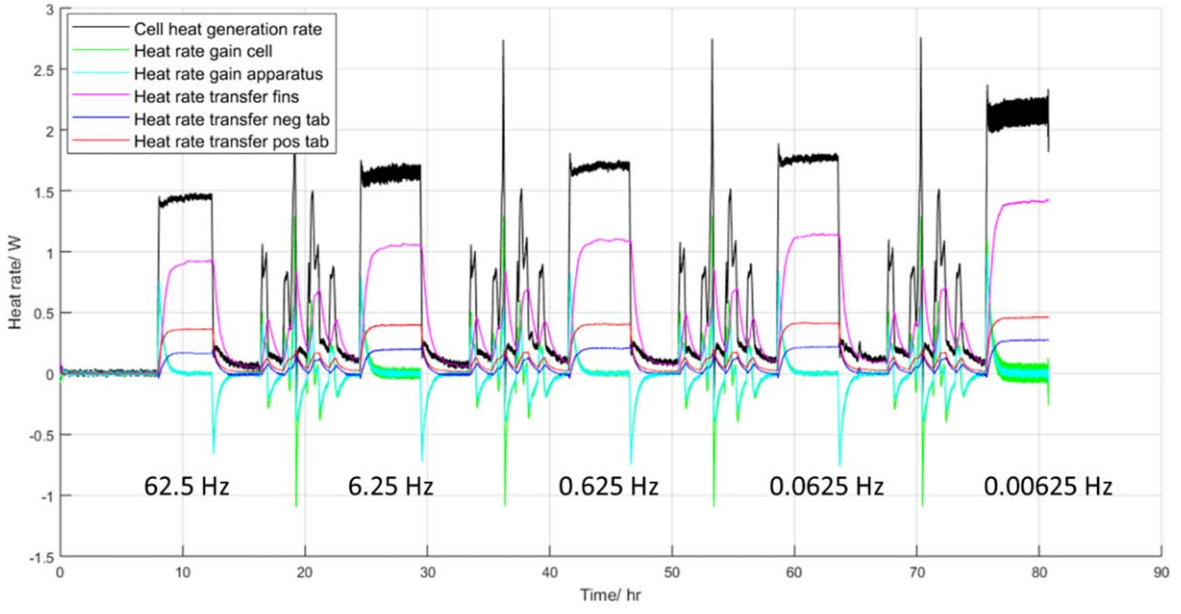

Figure 7. Heat generation rates observed with varying pulsing frequency.

heat rate dissipated through the negative tab (in blue), and (5) heat rate dissipated through the positive tab (in red). Most of the heat is dissipated through the cell surface, it is observed that about two thirds of the total heat generated is dissipated through the surface fins. This is expected as the area of the cell surface is much larger than the area of the tabs.

Figure 8 shows the trend on heat generation rate with increasing pulsing frequency in logarithmic scale. This heat generation rate—frequency map is characteristic of this particular cell, like a footprint. Whilst this map will differ from the maps obtained from cells with different chemistry, format or physical design, the overall trend observed aligns with the electrochemical principles governing lithium-ion batteries and will be common for all lithium-ion cells.

The heat generation map displayed in Fig. 8 suggest the presence of three regions, a low frequency region, a high frequency region and a distinct plateau region in the middle. The general trend observed is that the lower the frequency (longer pulses), the higher the heat generation. This can be explained by the influence of the mass transport and kinetic overpotentials on the heat generation rate at the different frequencies spanned.

Mass transport to or from an electrode can occur by three processes: convection and stirring, electrical migration in an electric potential gradient, and diffusion in a concentration gradient. Diffusion in the solid phase inside the particles as a result of a concentration gradient is a significant contribution towards heat generation at low frequencies. However, at very high frequencies (pulses with a duration less than milliseconds) diffusion in the solid phase will be negligible and the ion movement will be mainly due to movement of ions in the electrolyte (migration). Notably, the three regions displayed in Fig. 8 seem to correspond to the frequency ranges in which: (1) diffusion in the solid phase dominates mass transport (low frequency, high heat generation), (2) diffusion and migration coexist (plateau region) and (3) migration is dominant (high frequency, low heat generation).

The effects of (dis)charge pulses on lithium-ion batteries were evaluated before by many authors.[7,35–37] De Jongh et al. analysed the effects of the pulses on the internal processes such as diffusion, migration, electrochemical reactions and heat generation.[35] By using an electronic network model and experimental measurements they observed comparable trends at high, mid and low frequencies.

First, they compared high frequency charge pulses with constant current charge and observed that the total effective resistance to ion migration and diffusion in the electrolyte solution is significantly lower for pulsed than for direct current charging. This can be rationalised as follows: whilst during continuous charging (comparable to low frequencies) the Li^+ ions carry the current through the battery and the PF_6^- ions do not move after the concentration gradient is set-up, during short charge pulses (high frequency) both types of ions move. As the mobility of the PF_6^- ions is higher than that of the Li^+ ions, most of the pulse charged movement is carried by the PF_6^- ions. The resistance for charge movement for these PF_6^- ions is lower than that for the Li^+ ions. Consequently, the overall effective resistance to ion movement is lower for short pulses and so the heat generated. They also concluded that pulses shorter than the millisecond ($f > 1$ kHz) are completely buffered by the double layer capacitances at the electrode-electrolyte interphases and therefore the electrode potentials and reaction currents are virtually constant. These pulses led to instantaneous ion migration in the electrolyte and the concentration gradients are not significantly influenced. These observations align with the trend observed in Fig. 8 where less heat generation is noted for high frequencies.

De Jongh et al. also studied pulses in the mid and low frequency range where the kinetic overpotential and the mass transport overpotential dominated by diffusion play a role. For pulses at the mid frequencies (10–0.1 Hz in simulations and 1 kHz − 10 Hz experimentally) they observed a slow rise in voltage related to the electrode charge transfer reactions starting to adapt to the new current density. This slow increase or voltage plateau corresponds to the heat generation rate plateau observed at mid frequencies in Fig. 8. They also observed that concentration gradients within the battery only start changing on a time scale of seconds. For pulses longer than 10 s the voltage rise due to diffusion in the solid state becomes noticeable. Similarly, an increase in the heat generation rate at matching frequencies is observed in Fig. 8.

For further analysis of the trends observed in the heat generation —the frequency map from Fig. 8 is compared with the Bode plot (Fig. 9a) obtained from a galvanostatic EIS experiment performed at 0.1 C in the same cell. Figure 9a shows the real part of the impedance plotted with log frequency on the *X*-axis. The three frequency regions noticed in Fig. 8 are also present in Fig. 9a: I) low frequency region with high resistance, II) plateau region in the mid frequency range and III) high frequency region with low resistance. This correlates with the heat generation rates, the higher the resistance the higher the heat generation and vice versa.

We also tried to replicate the results obtained from the EIS experiment by repeating the heat generation measurement in similar conditions to the ones observed in the EIS experiment: pulsing at low C-rate (0.1 C instead of 2 C) for all frequencies, 25 °C and 50% SOC. We estimated the equivalent resistance (R_Q) from Eq. 10 and plotted it against frequency in Fig. 9b.

$$\dot{Q}_{\text{gen}} \approx \dot{Q}_{irrev} = I^2 \cdot R_Q(T, I, f) \qquad [10]$$

The current, I, in Eq. 10 is the measured current. At higher frequencies an increasing percentage of the current will be carried by charging/discharging the electrical double layer compared to a redox

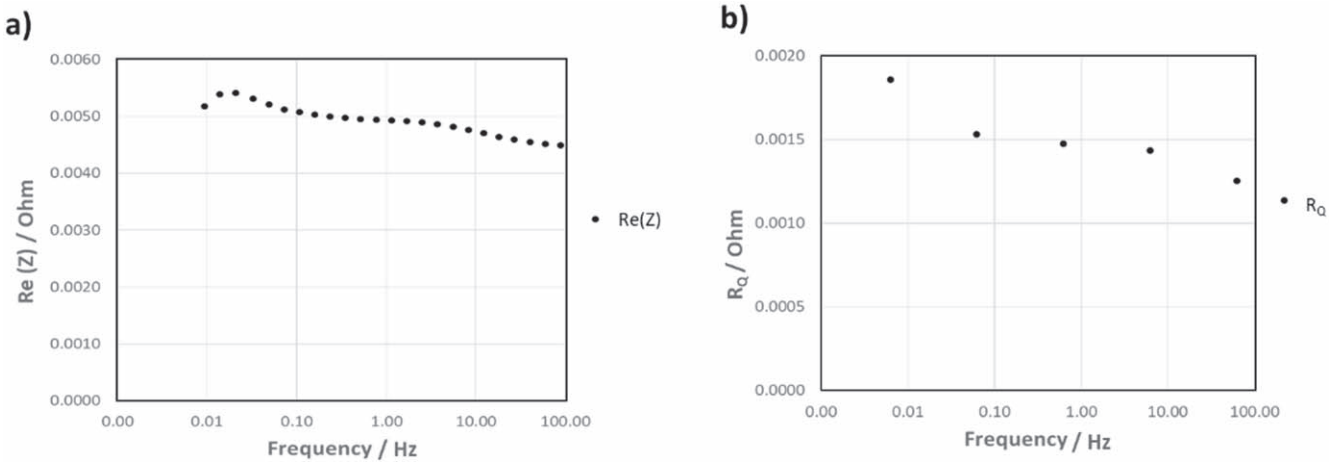

Figure 9. (a) EIS Bode plot performed at 0.1 C, (b) Approximated equivalent resistance vs frequency obtained from a pulsing experiment at 0.1 C using the apparatus.

process at the electrode surface. However, the square wave charge/discharge current profile is chosen so that the heat generation due to entropy, and the contribution from charging/discharging of the electrical double layer, cancels out. Therefore, the remaining heat generation will be almost entirely due to the enthalpy of the remaining processes, such as charge transfer and mass transfer. In order to obtain a complete picture of the thermal behaviour of a cell, the entropic behaviour of a cell must be known, but methods to measure the entropic coefficients of lithium-ion batteries are well known[38,39] and the purpose of this paper is to improve the measurement of the irreversible heat generation. To summarise, the heat generation decreases as frequency increases and less of the current is dependent upon charge transfer and mass transfer processes.

Whilst the trend observed in the resistance matched significantly the one from the EIS experiment the values were subjected to experimental error. This is because the apparatus was designed to measure heat generation rates at C-rates over 1 C. Therefore, using very low C-rates such as 0.1 C introduces substantial experimental error. Despite this we observed that the changes in the resistance and the plateau region occurs in the same frequency ranges for both experiments and agree with the heat generation map displayed in Fig. 8.

C-rate study.—One main variable when studying the heat generation rate from lithium-ion cells is the operating current. It can be anticipated from Eqs. 1 and 9 that the higher the operating current is, the higher the resulting heat generation will be - the heat generation rates increase with increasing C-rates.[14] Since the pulsing experiments are carried out at an approximately constant SOC (50%), we can assume the total heat generation is solely due to irreversible heat generation as described in Eq. 10. Consequently, we can expect something close to a squared relationship between operating current and heat generation. To evaluate this, the heat generation rate was measured using different pulsing amplitudes or C-rates.

The frequency (0.625 Hz), SOC (50%) and temperature (25°C), were all fixed for the following experiments (see Table I). Figure 10 shows the total heat generation rate measured in black, which is the sum of all the partial heat rates observed. We observed again that about two thirds of the heat generated is dissipated through the cell surface, dominating the total heat generation rate.

Figure 11 shows the trend in heat generation rate with increasing C-rate. As the C-rate increases, Joule heating (ohmic), which is the main heat source in the battery, increases proportionally to the square of I_{pulse}. The cell temperature also increases as the current increases (1.1 °C for 1 C, 3.8 °C for 2 C, 7.5 °C for 3 C). Although the resistance reduces during the temperature rise (see the Temperature study section), the heat generation rate is more sensitive to current because of the squared relationship in Eq. 10, which gives rise to a dramatic temperature growth inside the cell with the increment of current. We observed that distinctive squared relationship in Fig. 11.

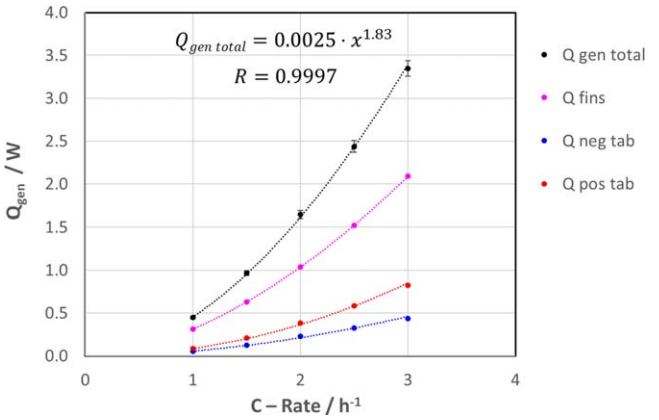

Figure 11. Heat generation rate vs C-rate.

The effects of varying pulsing current amplitude on cell temperature were also evaluated by Zhu et al. with similar observations.[36] Song et al. also evaluated the effect of C-rates on the heat generation rates during charge and discharge using an electrochemical thermal model.[9] They analysed the ratio from each heat source to the total heat generation and the differences between charge and discharge. Similarly, they observed that Joule heating, dominant heat source in the battery for C-rates over 0.1 C, increases proportionally to the squared of the applied current. Consequently, the charging or discharging time decreases. As a result, the total heat increases almost linearly as the C-rate increases. Regarding the ratio of the heat from each source as a function of C-rates, they observed that the entropic heat is seen to be the largest at a low C-rate (C-rate $\ll$ 0.1 C) but rapidly decreases as C-rate increases. This cannot be appreciated in our map since our apparatus does not quantify the reversible heat and therefore it is only accurate for C-rates over 0.1 C where irreversible heat sources become dominant.[40] Above 1.5 C, the ratio of irreversible heat sources is seen to be relatively constant

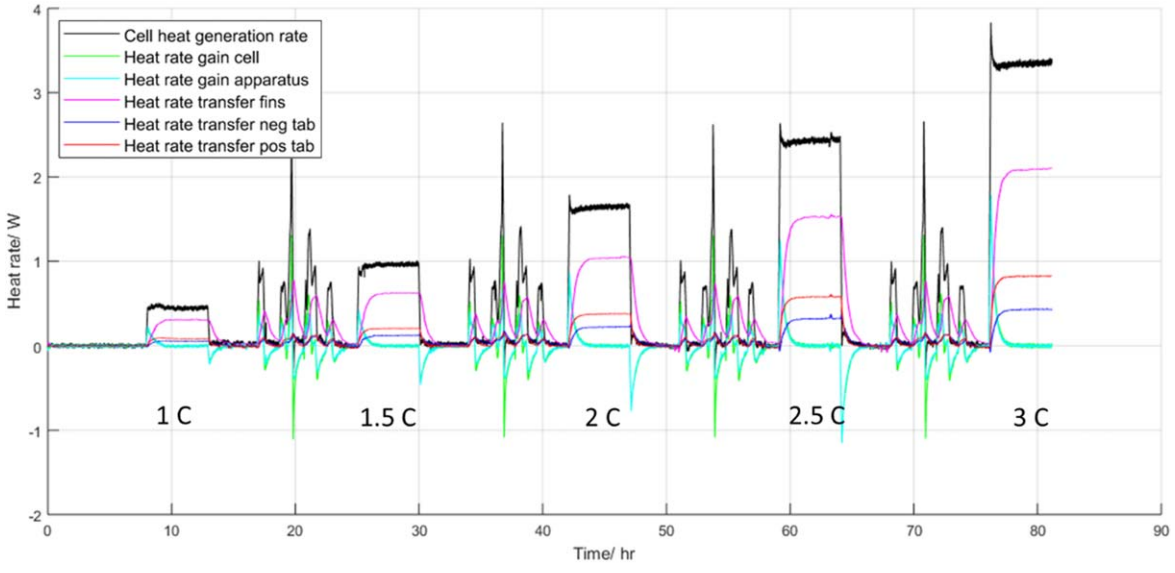

Figure 10. Heat generation rates observed with varying C-rate.

because the increasing rates of irreversible heat sources are identical. These observations validate our methodology.

SOC study.—Another variable that significantly influences the heat generation rate in a lithium-ion cell is the SOC. Recent work has shown that the internal resistance of the battery and associated heat generation rates change as a function of SOC.[6,9,41–45] The variation of heat generation rate with SOC is also linked to the entropic heat which is chemistry dependent and therefore influenced by the selection of the cathode and anode. To evaluate the heat generation-SOC relationship of our cell (NMC622—graphite), we measured the heat generation rate at several SOCs with our apparatus. We selected the mid frequency point (f = 0.625 Hz), 2 C and 25 °C to carry out the SOC study (see Table I). Figure 12 shows the total and partial heat generation rates measured with the apparatus at particular SOCs. The dominant heat generation rate contribution is again coming from the surface fins.

We can observe the trend on the heat generation rate with increasing SOC in Fig. 13. The heat generation rate remains constant at medium and high SOCs and decreases slightly for lower SOCs. According to Zhao et al. the ohmic resistance, measured by EIS, is not a strong function of SOC for an NMC 622 - graphite cell.[27] However, the diffusion impedance and charge transfer are increasing with decreasing SOC. We can observe this clearly in our heat generation map where the heat generation rate increases slightly for 20% SOC while remains relatively constant for all other higher SOCs.

Many authors have studied the influence of SOC on heat generation rates for different lithium-ion chemistries.[9,11,20,27,46] Recently, Song. et al. studied the profiles of the heat generation rates from each heat source (overpotentials, charge transport and entropic heat) during constant current charging and discharging at 2 C and 25 °C by using an electrochemical thermal model.[9] They observed that the most significant heat sources in a LMO-NMC - graphite cell have a different magnitude and tendency with SOC. In particular, the entropic heat was highly dependent on SOC and mirrored at charging and discharging because of its reversible nature. Additionally, the heat generation rate due to the difference of ion concentration within particles was also dependent on SOC and its magnitude was observed to be the largest, especially at low SOC during discharging. Furthermore, impedances measured by EIS have shown that the charge transfer resistance of the cell is the largest when the voltage is at 0% SOC.[47] This aligns with the conclusions

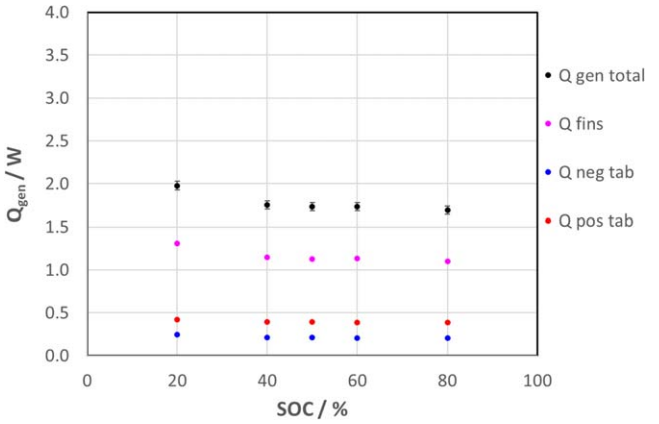

Figure 13. Heat generation rate vs state of charge.

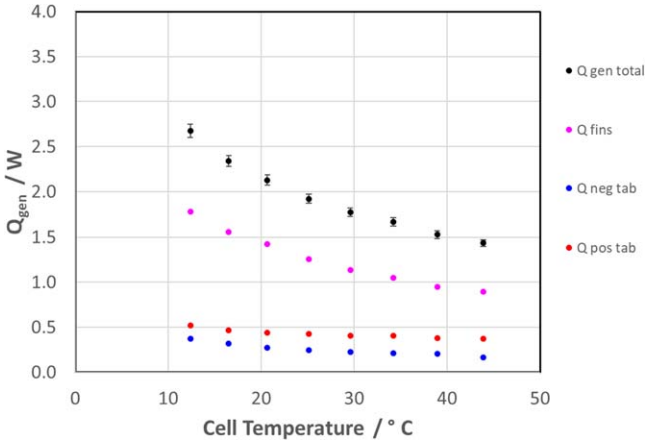

Figure 14. Heat generation rate vs temperature.

from Zhao et al. for an NMC622—graphite and the results from our heat generation map for a similar chemistry.[27] The values observed in the heat generation map are also in good agreement with those reported in the literature for a similar chemistry.[7,9,27]

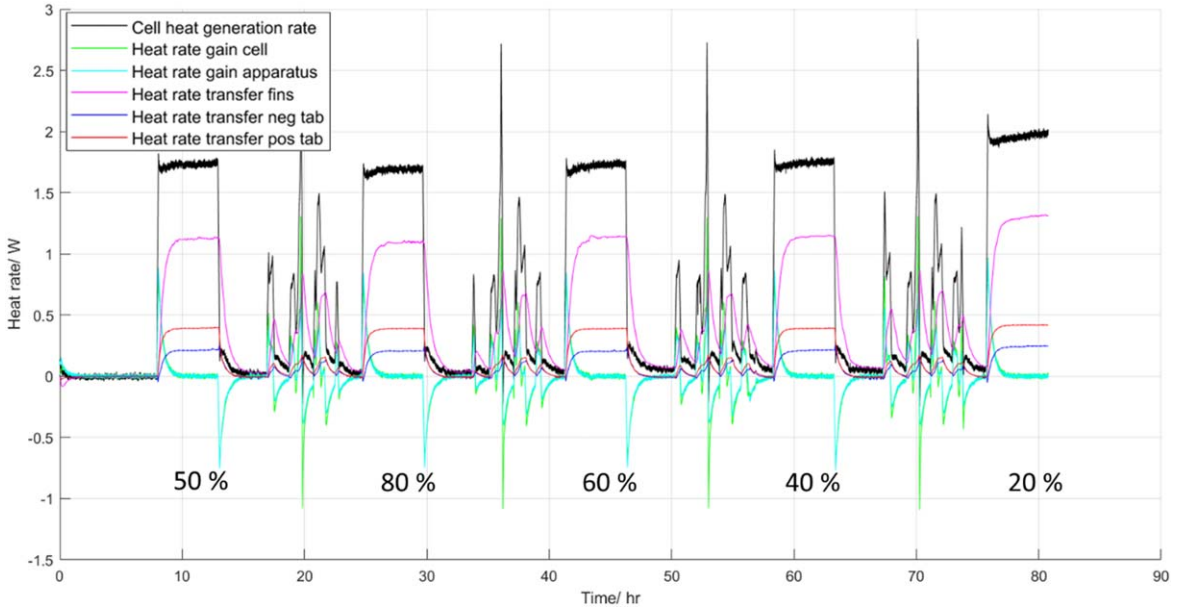

Figure 12. Heat generation rates observed at various SOCs.

Song et al. also studied the heat generation rate contributions from each cell component (cathode, anode, separator) and their relationship with SOC.[9] Assuming that the contact resistance at the interface of the anode and current collector is same as that of the cathode and current collector, they observed that the heat generation rate from the cathode, for both charging and discharging, had a peak at a low SOC. This is where the difference of ion concentration within particles is larger, which leads to a large potential difference. By contrast, the potential does not significantly change with the ion concentration for the anode. At the separator, the SOC dependency of the heat generation rate is similar, and the magnitude is small because the only heat generated is due to ion transport.

Temperature study.—Temperature plays a major role on the heat generation rate in a lithium-ion cell. Cell efficiency is related to the rate of the chemical reactions and physical processes which are governed by temperature.[9] All variables other than ambient temperature in the environmental chamber ($T_{control}$) were kept constant; frequency (0.625 Hz), pulse amplitude (2 C), and SOC (50%), see Table I. Figure 14 shows the trends in the heat generation rate - cell temperature map.

The total heat generation rate displays a clear exponential trend. This aligns with previous research concluding that the Arrhenius equation can reliably describe this relationship.[6,14,29,36,45,47–49] The two resistances (R_0 and R_{CT}) decrease exponentially with increasing temperature and the charge transfer resistance appears to dominate the cell impedance at low temperatures.[6,36] According to Arrhenius law the charge transfer resistance can be described by Eq. 11, where A is a pre-exponential constant, E_a is the activation energy, R the universal gas constant and T is temperature.

$$R_{CT}(T) = A \cdot \exp\left(\frac{E_a}{RT}\right) \quad [11]$$

It is important to note that the charge-transfer resistance is also current dependent. The electrode current reaction can be calculated from the Butler-Volmer (Eq. 5) and the overpotential of the intercalation reaction. In this experiment, we kept the current (pulse amplitude) constant to 2 C to highlight the influence of temperature on the heat generation rates. Regarding the ohmic resistance, the Arrhenius temperature dependence indicates that the ionic conductivity of the electrolyte is the major contribution to R_0. Low temperatures lead to high electrolyte viscosity and poor lithium-ion transport so higher resistance and therefore higher heat generation.

Song. et al. also studied the effect of temperature on the heat generation rates using an electrochemical thermal model.[9] The results showed that the most dominant heat source at high temperatures was the change of entropy because the battery internal resistance is small at high temperatures, resulting in low irreversible heat generation rates. However, it is important to note that there are cell models in which the internal resistance is high over a wide range of temperature, and therefore the irreversible heat could dominate even at high temperatures.[47,50,51] By contrast, the irreversible heat generation rapidly increases at low temperatures with the contributions from the contact resistance (ohmic), ion concentration difference within particles, and ion migration. The area of microcontact spots of the interface between active material particles and current collectors is caused by a deformation of materials and directly related to the material strength. At low temperatures, the material strength increases, and the deformation is reduced. Consequently, the contact area is reduced and therefore the contact resistance increases. Additionally, the gradient of ion concentrations in particles increases the charge transfer resistance at low temperatures.[47] Regarding ion transport, they observed that it becomes hindered at low temperatures and therefore the heat generation rate increases. These observations agree with the trends observed in our heat generation—temperature map. The values reported by Song. et al. are also in agreement with the ones observed in this investigation.[9]

SOH effects.—An important remark is that the heat generation rate maps obtained are only valid for comparison among cells when taken at beginning-of-life (BOL). As soon as a cell starts to degrade, impedance increases and so the heat generation. Depending on how this cell is degraded, e.g. ageing conditions which will determine which degradation mechanism is dominant, impedance increase will vary significantly and so the heat generation. As an example, we measured how the heat generation rate—C-rate maps changed for the same cell taken at different SOH. Figure 15a shows the heat generation rate—C-rate map when the cell studied has observed 4.4% capacity fade and Fig. 15b when the cell has observed 6.6% capacity fade. The heat generation rates have increased dramatically when the cell is further degraded. This phenomenon has been observed before in other studies, e. g. Liu et al. reported that the irreversible heat generation rate increases as the cell ages, and that the aging effect is more significant for charging process than discharging.[20]

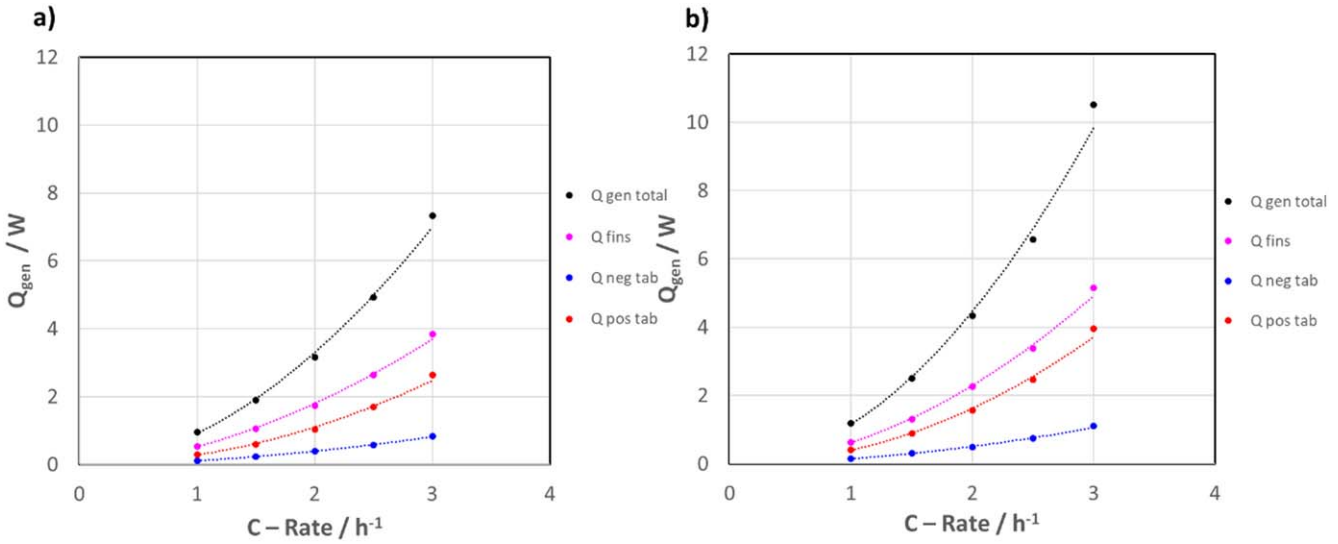

Figure 15. (a) Heat generation rate vs C-rate when the cell has suffered 4.4% capacity fade, (b) Heat generation rate vs C-rate when the cell has suffered 6.6% capacity fade.

Significance of the results: heat generation maps in application.—In order to select the right cell and design a good battery pack, it is necessary to be able to thermally manage those cells within the desired operating conditions. In order to do this it is necessary to know both how effectively heat can be removed from the cell and how much heat will be generated by the cell during operation. Our previous work on establishing the CCC[8] can now be combined with the heat generation maps described here as a design process for engineers.

First, we define the required thermal gradient, from the maximum temperature allowed in the cell (T_{cell}) to the necessary surface temperature that must be maintained by the thermal management system ($T_{TM\ surface}$). This can be determined as a function of the heat generation rate ($\dot{Q}_{gen}$) and the surface CCC (CCC_{surf}). This gradient is termed $\Delta T_{cell\ to\ surf}$ and is described by Eq. 12:

$$\Delta T_{cell\ to\ surf} = T_{cell} - T_{TM\ surface} = \frac{\dot{Q}_{gen}}{CCC_{surf}} \quad [12]$$

The CCC_{surf} of this cell was determined to be 2.15 $W \cdot K^{-1}$, following the methodology reported by Hales et al.[8] Figure 16 displays a relationship of the heat generation—cell temperature map at constant C-rate (black line with spheres) and the heat generation—C-rate map at constant ambient temperature (black line with xs), previously defined. This figure also shows two grey curves which represent the estimation of the heat generation rate with cell temperature at 1 and 3 C, using the maps. By way of example, letters A, B and C indicate three specific operating points with different values of C-rate. Using our proposed methods for analysis, the consequences of these operational conditions are summarised in Table II.

The peak operating temperature, T_{cell}, of the cells in the pack is required to be kept below 40 °C, a typical target for industry application. Using the map displayed in Fig. 16 and Eq. 12 we can calculate the $\Delta T_{cell\ to\ surf}$ and $T_{TM\ surface}$ for different operating conditions. Therefore, for operation point A ($T_{ambient}$ = 40.52 °C and C-rate = 2 C):

$$\Delta T_{cell\ to\ surf} = \frac{1.43}{2.15} = 0.66\ °C \quad [12a]$$

$$T_{TM\ surface} = 40 - 0.66 = 39.34\ °C \quad [13]$$

The surface of the cell must be kept 0.66 °C below the cell's required maximum operational temperature of 40 °C, and consequently must be cooled 1.18 °C below ambient temperature ($T_{ambient}$ = 40.52 °C).

By extrapolating the heat generation - temperature map to other C-rates according to the heat generation-C-rate map, we can estimate some extreme scenarios for the thermal management system, which are operation points B and C in Fig. 16, at lowest and highest C-rates, respectively. Table II shows the values of $\Delta T_{cell\ to\ surf}$ and $T_{TMsurface}$ calculated for operating points B and C. For operation point B, the cell must be cooled just 0.53 °C below ambient temperature ($T_{ambient}$ = 40.52 °C). By contrast, the cell must be cooled 1.97 °C below the ambient temperature for operation point C, the most demanding operation point. The difference in the demands from the thermal management system is summarised in Fig. 16 by the parameter dT.

It should be taken into account that the empirical methodology described in this study has some limitations. One of them is that the cell temperature is measured by thermocouples adhered at cell's outer surface, therefore introducing an error. There are some non-invasive ways to measure the internal temperature of a cell that could be implemented in future work.[50,52–55] Another limitation is that the methodology is based on the concept of generating electrochemical heat by passing a squared-wave current across the cell to keep the SOC constant at each operation point so only the irreversible heat generation rate is quantified, the entropic heat is not captured. Additionally, when using small C-rates experimental error can become significant since the measured thermal gradients are of a smaller magnitude. It should also be noted that the entropic heat is dominant at low C-rates, so it is not recommended using this methodology for very low C-rates (C-rate $\ll$ 0.5 C). In addition, the heat generation rate maps obtained are only valid for cell comparison when taken at the BOL. Future work should investigate degradation effects on the heat generation rates since the dominant degradation mechanism will play a role on the impedance increase and therefore in the heat generation rate.

Conclusions

An empirical method to measure the irreversible heat generation of a lithium-ion battery in the form of heat generation rate maps is

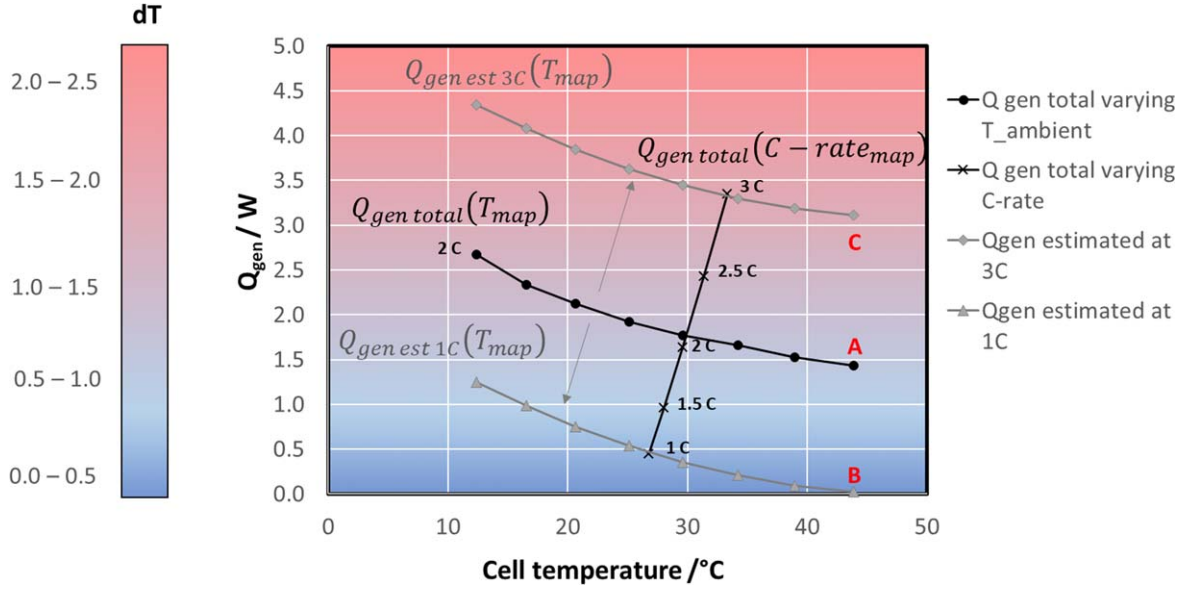

Figure 16. Combination of heat generation maps: heat generation rate vs cell temperature at constant C-rate (continuous black line with spheres), heat generation rate vs C-rate at constant ambient temperature (continuous black line with xs), estimated heat generation rate vs cell temperature at constant C-rate (grey lines).

Table II. Comparison of different operating points in terms of ambient temperatures, C-rates, heat generation rates, required thermal gradient and the necessary surface temperature provided by the thermal management system.

Operating point	Ambient temperature/°C	C-rate/h^{-1}	Cell heat rate/W	$\Delta T_{cell\ to\ surf}$/K	$T_{TM\ surface}$/°C
A	40.52	2	1.43	0.66	39.34
B	40.52	1	0.02	0.01	39.99
C	40.52	3	3.11	1.45	38.55

presented. Heat generation was measured as a function of frequency, current, state-of-charge (SOC) and temperature, resulting in 4D maps of heat generation. The results were highly consistent with previous literature on the subject. The heat generation maps can be informative on their own or combined with the cell cooling coefficient (CCC) and used for cell selection and as a design tool to define the requirements of the thermal management system for different operating conditions.

The rate of heat generation was most sensitive to current and temperature. Regarding current, the heat generation rate map showed a quadratic dependency, consistent with literature. In terms of temperature, lowering temperature rapidly increases the heat generation because of increased overpotentials. The exponential trend observed can be explained by the Arrhenius relationship of the ohmic and charge transfer resistances with temperature. The influence of frequency on the heat generation rate was noticeable, but less significant. Three major regions of behaviour were observed: (1) Low frequency region with high heat generation (diffusion dominated), (2) Plateau region (diffusion and migration coexist) and (3) High frequency region with low heat generation (migration dominated). Those regions align with the regions observed in the Bode plot for impedance obtained from an EIS experiment for the same cell. In terms of SOC, the map shows that the heat generation rate increases at very low SOCs, remaining constant at all other SOCs studied. This is due to the diffusion impedance and charge transfer resistance increasing with decreasing SOC. This is not expected to be the same for every cell as it will be a function of the materials and electrode balancing.

Finally, a worked example is set out to demonstrate how the obtained heat generation maps can be used in combination with the CCC in the early stages of a battery pack thermal management system design. Three operational points at differing C-rate were compared in terms of heat generation rates and the requirements needed from the thermal management system. The heat generation maps are easily obtained with the described empirical methodology using equipment that can be found in most electrochemical labs. They provide an insight into the thermal performance of the cell across a desired range of operation conditions. The validity of the observations in the heat generation maps holds beyond the specific choice of electrode materials, geometry and physical design, as long as physicochemical interactions are of a similar nature. Therefore, the methodology can be applied to evaluate any lithium-ion cell, independently of its chemistry, format or physical design. Consequently, battery pack designers will gain a valuable technique enabling cell to cell comparison from a thermal perspective in order to select the most appropriate cell for an application. The uptake of the heat generation maps by cell manufacturers and its inclusion on the specification sheets would inform their potential customers on the thermal performance of their cells enhancing competition, not only competing on power and energy density criteria.

The present study provides heat generation maps as a tool alongside the cell cooling coefficient to summarise how easy or hard it is to thermally manage any type of cell in any type of application. This is a critical advancement. Uptake of the methodology will allow engineers within the battery industry to optimize thermal management systems with a simple analysis method at a much earlier stage in battery pack design than was previously possible, saving considerable time and money. A better understanding of how easy or hard it is to thermally manage cells could also incentivise cell manufacturers to optimise both heat rejection and heat generation together. In the authors opinion, comparison drives competition, and manufacturers who can offer the best cell thermal performance (optimal heat rejection and low heat generation) will gain a competitive advantage, those who ignore do so at their peril.

Acknowledgments

This work was supported by the Faraday Institution (grant number EP/S003053/1, FIRG003), the Innovate UK THT project (grant number 105297), the Innovate UK BATMAN project (grant number 491 104180), the Innovate UK CoRuBa project (133369), and the EPSRC TRENDS project (grant number 492 EP/R020973/1).

ORCID

Laura Bravo Diaz https://orcid.org/0000-0002-0259-8590
Alastair Hales https://orcid.org/0000-0001-6126-6986
Mohamed Waseem Marzook https://orcid.org/0000-0003-4430-7322
Yatish Patel https://orcid.org/0000-0001-7828-5315
Gregory Offer https://orcid.org/0000-0003-1324-8366

References

1. G. E. Blomgren, *J. Electrochem. Soc.*, **164**, A5019 (2017).
2. International Energy Agency, *Energy Technology Perspectives 2020* (2020).
3. International Energy Agency, (2020), (https://iea.org/reports/tracking-transport-2020. Available at: https://iea.org/reports/tracking-transport-2020). (Accessed: 1st September 2021).
4. J. Francfort and K. Walkowicz, *US Drive Electrochemical Energy Storage Technical Team Roadmap*, p. 1 (2017).
5. G. Offer, Y. Patel, A. Hales, L. Bravo Diaz, and M. Marzook, *Nature*, **582**, 485 (2020).
6. Y. Troxler, W. Bu, M. Marinescu, V. Yufit, Y. Patel, A. J. Marquis, N. P. Brandon, and G. J. Offer, *J. Power Sources*, **247**, 1018 (2014).
7. A. Hales, L. Bravo Diaz, M. W. Marzook, Y. Zhao, Y. Patel, and G. J. Offer, *J. Electrochem. Soc.*, **166**, A2383 (2019).
8. A. Hales, M. W. Marzook, L. Bravo Diaz, Y. Patel, and G. J. Offer, *J. Electrochem. Soc.*, **167**, 020524 (2020).
9. M. Song, Y. Hu, S.-Y. Choe, and T. R. Garrick, *J. Electrochem. Soc.*, **167**, 120503 (2020).
10. D. Bernardi, *J. Electrochem. Soc.*, **132**, 5 (1985).
11. T. M. Bandhauer, S. Garimella, and T. F. Fuller, *J. Electrochem. Soc.*, **158**, R1 (2011).
12. H. Liu, Z. Wei, W. He, and J. Zhao, *Energy Convers. Manag.*, **150**, 304 (2017).
13. C. Heubner, M. Schneider, and A. Michaelis, *J. Power Sources*, **307**, 199 (2016).
14. A. N. Mistry, K. Smith, and P. P. Mukherjee, *ACS Appl. Mater. Interfaces*, **10**, 28644 (2018).
15. Y. Lai, S. Du, L. Ai, L. Ai, and Y. Cheng, *Int. J. Hydrogen Energy*, **40**, 13039 (2015).
16. L. Bravo Diaz, X. He, Z. Hu, F. Restuccia, M. Marinescu, J. Varela Barreras, Y. Patel, G. J. Offer, and G. Rein, *J. Electrochem. Soc.*, **167**, 090559 (2020).
17. C. Y. Wang and V. Srinivasan, *J. Power Sources*, **110**, 364 (2002).
18. B. Wu, V. Yufit, M. Marinescu, G. J. Offer, R. F. Martinez Botas, and N. P. Brandon, *J. Power Sources*, **243**, 544 (2013).
19. A. Nazari and S. Farhad, *Appl. Therm. Eng.*, **125**, 1501 (2017).
20. G. Liu, M. Ouyang, L. Lu, J. Li, and X. Han, *J. Therm. Anal. Calorim.*, **116**, 1001 (2014).
21. K. Chen, G. Unsworth, and X. Li, *J. Power Sources*, **261**, 28 (2014).
22. S. J. Drake, M. Martin, D. A. Wetz, J. K. Ostanek, S. P. Miller, J. M. Heinzel, and A. Jain, *J. Power Sources*, **285**, 266 (2015).
23. A. Hales, R. Prosser, L. Bravo Diaz, G. White, Y. Patel, and G. J. Offer, *Etransportation*, **6**, 100089 (2020).
24. K. W. Beard and T. B. Reddy, *Linden's Handbook of Batteries*, ed. K. W. Beard and T. B. Reddy (McGraw-Hill Education, New York, NY) (2019).

25. R. O'Hayre, S.-W. Cha, W. G. Colella, and F. B. Prinz, *Fuel Cell Fundamentals* (Wiley, New Jersey, NJ) (2016).
26. A. J. Bard, L. R. Faulkner, E. Swain, and C. Robey, *Electrochemical Methods Fundamentals and Applications.*, .
27. W. Zhao, M. Rohde, I. U. Mohsin, C. Ziebert, and H. J. Seifert, *Batteries*, **6**, 1 (2020).
28. N. Meddings et al., *J. Power Sources*, **480** (2020).
29. D. Andre, M. Meiler, K. Steiner, C. Wimmer, T. Soczka-Guth, and D. U. Sauer, *J. Power Sources*, **196**, 5334 (2011).
30. E. Barsoukov, J. H. Jang, and H. Lee, *J. Power Sources*, **109**, 313 (2002).
31. M. Fleckenstein, S. Fischer, O. Bohlen, and B. Bäker, *J. Power Sources*, **223**, 259 (2013).
32. P. Keil, K. Rumpf, and A. Jossen, *World Electr. Veh. J.*, **6**, 581 (2013).
33. M. Swierczynski, D. I. Stroe, T. Stanciu, and S. K. Kær, *J. Clean. Prod.*, **155**, 63 (2017).
34. W. Weppner and R. A. Huggins, *J. Electrochem. Soc.*, **124**, 1569 (1977).
35. P. de Jongh and P. H. L. Notten, *Solid State Ionics*, **148**, 259 (2002).
36. Z. Jiangong Zhu, X. Sun, Wei, and H. Dai, *Int. J. Energy Res.*, **40**, 1869 (2016).
37. Q. Li, S. Tan, L. Li, Y. Lu, and Y. He, *Sci. Adv.*, **3**, 1701246 (2017).
38. L. Cells, P. J. Osswald, J. Garche, A. Jossen, and H. E. Hoster, *Electrochim. Acta*, **177**, 270 (2015).
39. X. F. Zhang, Y. Zhao, Y. Patel, T. Zhang, W. M. Liu, M. Chen, G. J. Offer, and Y. Yan, *Phys. Chem. Chem. Phys.*, **19**, 9833 (2017).
40. S. Gross, *Energy Convers.*, **9**, 55 (1969).
41. D. Aurbach, M. D. Levi, E. Levi, H. Teller, B. Markovsky, G. Salitra, U. Heider, and L. J. Heider, *J. Electrochem. Soc.*, **145**, 3024 (1998).
42. J. Hong, H. Maleki, S. Al Hallaj, L. Redey, and J. R. Selman, *J. Electrochem. Soc.*, **145**, 1489 (1998).
43. W. Lu and J. Prakash, *J. Electrochem. Soc.*, **150**, A262 (2003).
44. S. Skoog, *Conf. Proc. - IEEE Appl. Power Electron. Conf. Expo. - APEC*(IEEE) pp.2369 (2017).
45. I. Jiménez Gordon, S. Grugeon, A. Débart, G. Pascaly, and S. Laruelle, *Solid State Ionics*, **237**, 50 (2013).
46. K. Onda, H. Kameyama, T. Hanamoto, and K. Ito, *J. Electrochem. Soc.*, **150**, A285 (2003).
47. S. S. Zhang, K. Xu, and T. R. Jow, *Electrochim. Acta*, **49**, 1057 (2004).
48. H. M. Cho, W. S. Choi, J. Y. Go, S. E. Bae, and H. C. Shin, *J. Power Sources*, **198**, 273.
49. T. Momma, M. Matsunaga, D. Mukoyama, and T. Osaka, *J. Power Sources*, **216**, 304 (2012).
50. J. G. Zhu, Z. C. Sun, X. Z. Wei, and H. F. Dai, *J. Power Sources*, **274**, 990 (2015).
51. T. Osaka, D. Mukoyama, and H. Nara, *J. Electrochem. Soc.*, **162**, A2529 (2015).
52. J. P. Schmidt, S. Arnold, A. Loges, D. Werner, T. Wetzel, and E. Iveers-Tiffee, *J. Power Sources*, **243**, 110 (2013).
53. R. R. Richardson, P. T. Ireland, and D. A. Howey, *J. Power Sources*, **265**, 254 (2014).
54. N. S. Spinner, C. T. Love, S. L. Rose-Pehrsson, and S. G. Tuttle, *Electrochim. Acta*, **174**, 488 (2015).
55. C. Zhang, K. Li, and J. Deng, *J. Power Sources*, **302**, 146 (2016).